photonics

MDPI

Article

Integration of Single-Photon Sources and Detectors on GaAs

Giulia Enrica Digeronimo *, Maurangelo Petruzzella, Simone Birindelli, Rosalinda Gaudio, Sartoon Fattah Poor, Frank W.M. van Otten and Andrea Fiore

Department of Applied Physics, Eindhoven University of Technology, P.O. Box 513, 5600 MB Eindhoven, The Netherlands; m.petruzzella@tue.nl (M.P.); s.birindelli@tue.nl (S.B.); rosalinda.gaudio@gmail.com (R.G.); sartoon.fattahpoor@gmail.com (S.F.P.); F.W.M.v.Otten@tue.nl (F.W.M.v.O.); a.fiore@tue.nl (A.F.)

* Correspondence: g.e.digeronimo@tue.nl; Tel.: +31-402-475-057

Received: 13 September 2016; Accepted: 16 October 2016; Published: 21 October 2016

Abstract: Quantum photonic integrated circuits (QPICs) on a GaAs platform allow the generation, manipulation, routing, and detection of non-classical states of light, which could pave the way for quantum information processing based on photons. In this article, the prototype of a multi-functional QPIC is presented together with our recent achievements in terms of nanofabrication and integration of each component of the circuit. Photons are generated by excited InAs quantum dots (QDs) and routed through ridge waveguides towards photonic crystal cavities acting as filters. The filters with a transmission of 20% and free spectral range $\geq$66 nm are able to select a single excitonic line out of the complex emission spectra of the QDs. The QD luminescence can be measured by on-chip superconducting single photon detectors made of niobium nitride (NbN) nanowires patterned on top of a suspended nanobeam, reaching a device quantum efficiency up to 28%. Moreover, two electrically independent detectors are integrated on top of the same nanobeam, resulting in a very compact autocorrelator for on-chip $g^{(2)}(\tau)$ measurements.

Keywords: quantum photonics integrated circuits; superconducting single photon detectors; quantum dots; photonic crystals cavities

1. Introduction

Quantum information processing (QIP) is a well-established scientific field that opens unconventional perspectives for information processing. QIP uses quantum bits (qubits) as units of information. While qubits can be based on atomic and solid state systems, photons have emerged as a promising approach for QIP [1]. However, it is very challenging to implement quantum processing functionalities on a large scale with bulk optics due to the extreme stability requirements and large coupling losses. The concept of quantum photonic integration [2] has been investigated as a scalable approach to photonic QIP, in principle enabling experiments with a few tens of photons. In order to realize a fully-functional quantum photonic integrated circuit (QPIC), all the required quantum optical components, such as single-photon sources, passive circuit elements, and single-photon detectors, must be integrated on a single chip. The use of III-V materials, especially GaAs and InP compounds, is very promising for QPIC [3] because it allows the integration of on-demand single-photon sources. Semiconductor quantum dots (QDs) have been shown to be nearly ideal sources of non-classical light [4] that can be efficiently routed into nanophotonic circuits [5–8]. As compared to integrated single-photon sources based on parametric processes in $LiNbO_3$ [9] or Si waveguides [10], QDs offer the advantage of much higher efficiency and easier filtering of the pump beam. Moreover, approaches to reproducibly control the exciton and cavity energy on chip, as needed to realize a scalable circuit, have been developed [11–14]. On the other side, superconducting single photon detectors (SSPDs) [15] based on niobium nitride (NbN) nanowires combine high detection efficiency, low dark count rates,

and ultra-fast response, making them promising candidates for QIP [16]. The integration of such detectors into nanophotonic circuits has been proved on different platforms: on GaAs with waveguides [17] and QDs [18], and on Si with waveguides [19] and nanobeam cavities [20]. Particularly in [18], the possibility of on-chip detection of the QDs emission light has been proved; however, the demonstrated circuit lacked more complex structures (high-finesse nanocavities, beam splitters, etc.) needed for photonic QIP.

Here, we present a prototype architecture of a fully integrated photonic quantum circuit on a GaAs platform (Figure 1), consisting of InAs QDs, photonic crystal waveguides (PhCWGs) and cavities (PhCCs), and SSPDs patterned on top of suspended nanobeams (SNBs). Thanks to the addition of PhCCs and PhCWGs, the emission from one or several QDs can be filtered on-chip so that single photons originating from a single excitonic line are funneled to circuits and then measured. We choose to integrate the superconductive nanowires on top of a SNB instead of a ridge waveguide since shorter lengths are sufficient to reach high absorption due to a tighter field confinement [21]. This is expected to reduce the role of wire inhomogeneities [22] and increase efficiency. Moreover, it is possible to place two electrically independent detectors on top of the SNB, such that the same guided mode is probed by the two SSPDs [23]. The autocorrelators together with the PhC filters would, for example, allow the performance of a Hanbury-Brow-Twiss (HBT) experiment [24] completely on-chip, which would be a meaningful validation of a fully functional QPIC. However, the integration of these different functionalities on the same platform shows significant technological challenges. In this paper, a low-temperature fabrication process that allows for the integration of the different components of the above-mentioned circuit is presented. Further, the characteristics and functionalities of each component (SSPDs, QDs and PhC filters) of the circuit fabricated at low temperature are shown in detail, and it will be demonstrated how the required functionality and performance is obtained for each component.

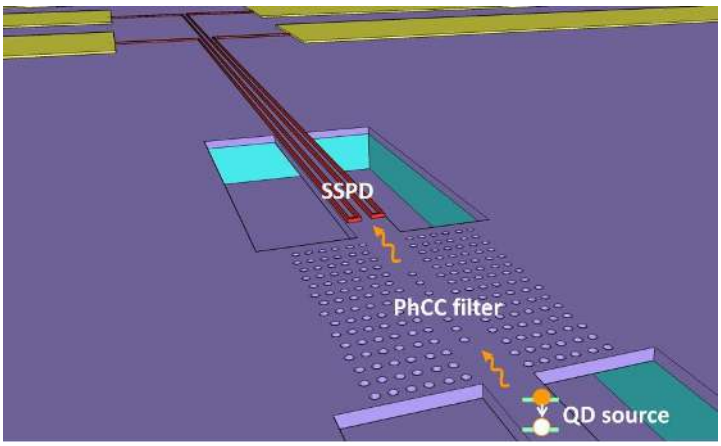

Figure 1. Sketch of the proposed approach for the quantum photonic integrated circuits (QPIC). Single photons are produced via spontaneous emission of excitons in quantum dots (QDs), efficiently funneled in waveguides, filtered by a photonic crystal cavity (PhCC) and detected by waveguide superconducting single photon detectors (SSPDs).

2. Materials and Methods

The fabrication process starts with the sputtering of a thin NbN film on top of the substrate for the fabrication of the SSPDs. In this step, it is crucial to have a substrate's surface with very low roughness (<0.5 nm), since the internal quantum efficiency of the detector depends on the quality and uniformity of the superconducting film [25]; consequently, a rough film could produce an inefficient SSPD. Therefore, it is crucial to start from a GaAs/AlGaAs heterostructure featuring very low roughness despite the QDs embedded inside. The sample is grown by molecular beam epitaxy on an undoped

GaAs substrate where a layer of GaAs with a 320 nm thickness including low-density InAs QDs [26] is grown on top of a 1.5-μm-thick layer of $Al_{0.7}Ga_{0.3}As$. At the end of the growth, an extra final step of deposition of a few atomic layers of GaAs, at 20 °C above the oxide removal temperature (585 °C) under an As flux, yields samples with a smooth surface (root mean square roughness = 0.4 nm). After the growth, a 5-nm-thick NbN film is deposited on top of the wafer by means of direct current reactive magnetron sputtering. A Nb target in Ar + N_2 mixture at total pressure P_{TOT} = 2.3 mTorr is sputtered for the deposition of the film. The deposition is carried out at a nominal temperature of 400 °C, with a target current of 250 mA and a target voltage of 380 V, conditions similar to those previously used to fabricate high-performance waveguide SSPDs [22]. This annealing step at 400 °C does not significantly change the emission spectra of the QDs, which display only a 5 nm blue shift after the sputtering process. The contact pads and alignment markers, consisting of 14 nm Ti and 140 nm Au layers, are defined through optical lithography, electron beam evaporation, and lift-off. The nanowires are patterned by electron beam lithography on a 100-nm-thick mask of hydrogen silsequioxane (HSQ) and then transferred to the NbN film via reactive ion etching (RIE) in an Ar/SF_6 plasma. Figure 2a shows a scanning electron microscopy (SEM) image of an etched wire (100 nm width, 160 nm pitch, and 20 μm length) covered with the HSQ mask. As can be noticed, the design was adjusted in the areas close to the corners in order to avoid current crowding around sharp edges [27]. In order to obtain high quality photonic crystal structures, the pattern has to be etched through a hard mask, which is usually made of a thick SiN film (200–400 nm) deposited at high temperature (300 °C) via plasma enhanced chemical vapor deposition (PECVD). However, in this specific case, to preserve the NbN quality film, it is essential to avoid thermal stress, and for this reason it is important that temperatures above 200 °C are never reached. A low-temperature recipe (70 °C) for the deposition of a 400 nm SiN hard mask has been used based on an induced coupled plasma (ICP) PECVD. A 320-nm-thick layer of ZEP520A as electron beam resist is deposited in the next step, and the design including the RWGs, the PhCs structures, and the SNBs is exposed with electron beam lithography, taking special care on the alignment of the wires with the SNB. Two subsequent RIE steps at room temperature are performed in order to etch through the SiN and GaAs layers. The higher density and different composition of the LT SiN hard mask required an optimization of the composition of the reactive gases; specifically, a CHF_3/O_2 plasma is used for the SiN etching, and a $SiCl_4$ plasma for the GaAs etching. The sacrificial AlGaAs layer is removed via wet etching in an HCl-based solution, which results in a geometrically well-defined etching profile due to different etching rates in different crystallographic orientations in AlGaAs [8]. A final step of dry etching to remove the residual SiN hard mask is usually required in order to open the metal contacts. However, it has been noticed that in this step the nanowires endure significant damage due to a lateral etching that drastically reduces the width of the wire and, correspondingly, the value of the critical current. An intermediate step of optical lithography and SiN etching has been added in order to open only the metal contact, avoiding the SiN etching in the active parts of the circuit. The SiN layer (50 nm) left on top does not seem to significantly modify the optical properties of the PhC structures (Figure 2b). Indeed, the quality factor (Q) of a cavity fabricated with this recipe is around 1000, as expected from the simulation for the chosen design. An example of a complete QPIC is presented in Figure 2 in which its different parts are visible: (a) the nanowire placed on top of a 15-μm-long, 1-μm-wide nanobeam, the two PhC waveguides with the PhC cavity and (b) the other SNB that is tapered to a RWG with a 5 μm width at the cleaved facet.

The electro-optical characterization of SSPD is performed at an estimated sample temperature of 2.3 K in a continuous flow helium cryostat. During the electrical measurements, the detector is biased through the DC port of a bias-T with a voltage source connected in series with a 10 Ω bias resistor. The RF port of the bias-T is instead connected to a 50 Ω cap. The electrical contact with the device is established with a 50 Ω microwave probe connected to the circuit through a SMA coaxial cable. During the optical measurement, the 50 Ω cap is removed and a 4 dB attenuator connected to a series of four amplifiers is now added to the RF port of the bias-T. A continuous wave 1300 nm diode laser is sent through a polarization-maintaining lensed fiber into the waveguides, and the detector

output signal coming from the amplifiers is then sent to a counter. Both the lensed fiber and the contact probes are mounted on piezoelectric positioners, which are thermally anchored to the cold plate to minimize the thermal load to the detector. The QDs and the PhC filters are characterized through the use of a non-resonant pump laser (780 nm) that is focused by a microscope objective (NA 0.4) into the sample to excite the QDs. The photoluminescence (PL) signal is collected from the end facet of the RWG through the lensed fiber, sent to a spectrometer (focal length = 1 m) and detected by an InGaAs array detector. All simulations both for the detectors and the filters are performed using a finite-element mode solver (COMSOL Multiphysics).

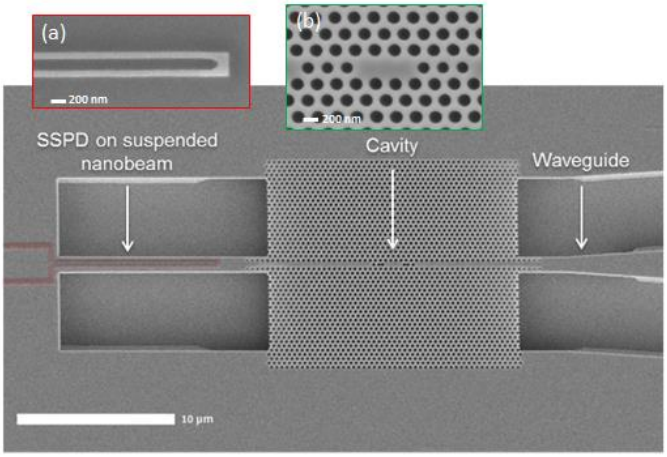

Figure 2. Scanning electron microscopy (SEM) picture of the full QPIC. Zoomed pictures of SSPD (**a**) and PhCC (**b**).

3. Results

3.1. Detectors

3.1.1. Design

The chosen design for the detectors on top of a SNB is based on simulations in which the absorptances for nanowires on top of either GaAs waveguides or nanobeams are compared. In the first design, an NbN meander (5-nm-thick, 100-nm-wide, and with a 250 nm pitch) was placed on top of a GaAs/$Al_{0.7}Ga_{0.3}As$ waveguide (1.85-µm-wide and 250-nm-deep). Assuming a complex NbN reflective index $\tilde{n}_{NbN} = 4.35 - i4.65$, the absorption coefficients for TE and TM polarizations provide a total absorptance of 84% and 82% for a 50-µm-long waveguide, respectively [21]. While the theoretical calculations suggest a high absorptance, the experimental device detection efficiency for this detector's design does not go above 20% [17], indicating that the inhomogeneities [22] could play a major role on limiting the detector's efficiency. Therefore, a new design, with a NbN meander on top of a GaAs SNB surrounded by air, has been proposed as a possible improvement [21]. As the index contrast between GaAs and the bottom cladding layer is higher as compared to the previous design, the field is pushed towards the top GaAs/NbN interface and the absorptance is improved. For the simulation, a NbN meander (5-nm-thick, 100-nm-wide nanowire with a 160 nm pitch) on top of a 1-µm-wide and 300-nm-thick SNB is considered. A 100-nm-thick HSQ film (amorphous silicon oxide) remaining on top of the nanowires after processing, as well as a residual 50-nm-thick SiN layer, are taken into account during the simulation. The absorption coefficients for TE and TM polarizations at 1310 nm are calculated as $\alpha_{TE} = 1166\ cm^{-1}$ and $\alpha_{TM} = 1399\ cm^{-1}$, by using the same $\tilde{n}_{NbN}$ as in [21]. The fundamental TE mode, the only interesting one in terms of integration with the QD sources, is presented in Figure 3. From the calculation, a 15 µm NbN nanowire on top of

a 7.5 µm SNB is already long enough to guarantee that 90% of the input light is absorbed, resulting in a lower probability of suffering of inhomogeneities.

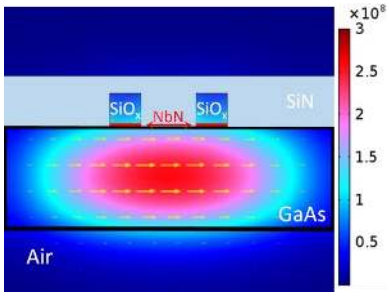

Figure 3. Simulated amplitude (V/m) and direction of the electric field for the fundamental mode of a suspended nanobeam (SNB) with a top niobium nitride (NbN) wire.

3.1.2. Performance

NbN SSPDs were fabricated on top of GaAs SNBs following the design in Figure 3 and the fabrication procedure presented in Section 2. In what follows, their performance at a low temperature (2.2 K) in terms of quantum efficiency, dead time, and jitter is discussed. A preliminary measurement to quickly judge the quality of an SSPD is the current-voltage (I-V) characteristic. The inset of Figure 4a displays the current-voltage characteristic measured for a 20-µm-long wire, showing a critical current (I_c) of 8 µA.

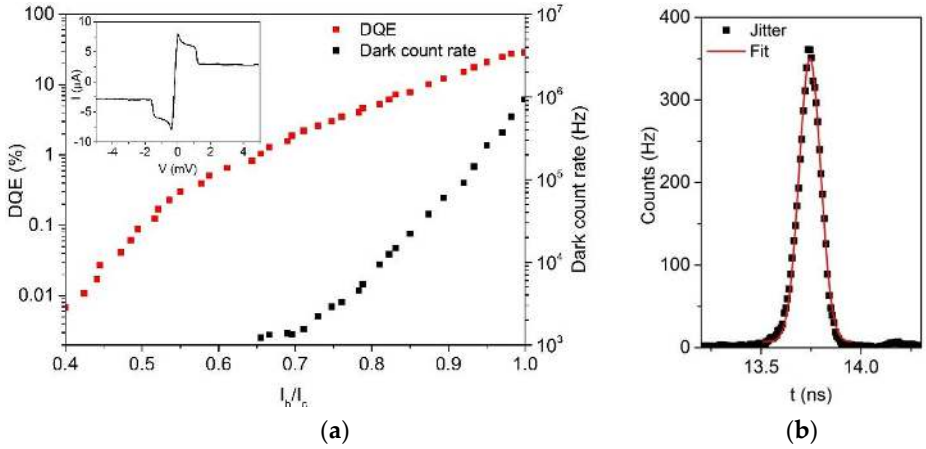

Figure 4. (**a**) Device quantum efficiency (DQE) (red) of a 20 µm-long SSPD on top of SNB under illumination at 1300 nm, and dark count rate (black) as a function of the normalized bias current. Inset: current-voltage characteristic. (**b**) Histogram of the jitter time of the detector biased 94% I_c.

The device quantum efficiency (DQE) is plotted in red Figure 4a as a function of the normalized bias current I_b/I_c, and it is defined as the number of counts minus the dark counts (in black) divided by the number of photons coupled to the waveguide. We note that the dark counts shown in Figure 4a have been measured in a cryostat with an optical window. They are therefore mostly produced by the absorption of infrared thermal photons and not indicative of the detector's performance in an optimized environment. The number of photons coupled into the ridge waveguide is determined by transmission measurements: the ratio of fiber-in to fiber-out averaged over a 2 nm spectra around 1300 nm gives a value of T = 0.06%, meaning that the coupling efficiency from the fiber to the center of the RWG is $\eta_C = \sqrt{T} = 2.5\%$, including the loss. Taking this η_c into account, the maximum value reached for the DQE is 28%. While the coupling efficiency is relatively low, due to the unoptimized

modal matching between the lensed fiber and the waveguide, the DQE is the relevant figure of merit for integrated experiments where the photons are produced within the chip.

The timing resolution (jitter) of a detector can be determined illuminating the detector with a pulsed laser (λ = 965 nm, 100 ps pulse width) and sending the output pulse to a correlation card together with the laser trigger signal to record the coincidences counts. Figure 4b shows the coincidence peak using a bias current of 94% I_c. The fit with a Gaussian distribution gives a full width half maximum (FWHM) value of 127 $\pm$ 8 ps. This value is much shorter than the QD carrier lifetime (~1 ns), so correlation measurements are not going to be significantly affected by the detector jitter. The analysis of the SSPD output pulse provides a value of FWHM = 3.4 ns and a 1/e decay time of 3.7 ns, which corresponds very well to the expected time constant $\tau = L_{Kin}/R$ for a value of wire kinetic inductance L_{Kin} = 180 nH, calculated from the kinetic inductance per square of the NbN wire L = 90 pH/□ [28].

3.1.3. Autocorrelator Performance

As already mentioned, the addition of a second independent detector on top of the SNB provides a very compact autocorrelator and opens the way to on-chip $g^{(2)}(\tau)$ measurements. In order to test the performance of the autocorrelators, two electrically independent detectors have been fabricated on top of a SNB that is tapered to a RWG. The close packing of the nanowires could in principle produce electrical, magnetic, or thermal coupling between the two detectors. In the following, we prove the absence of any crosstalk, either static or dynamic, between the two detectors on a single nanobeam, following a similar approach used in [23]. An initial series of tests is performed in static conditions to determine whether the bias condition of one detector has an influence on the electrical response of the other. Figure 5a shows the I-V characteristic of one detector (A) when the other one (B) is biased above the I_c or when it is not biased at all, and vice versa.

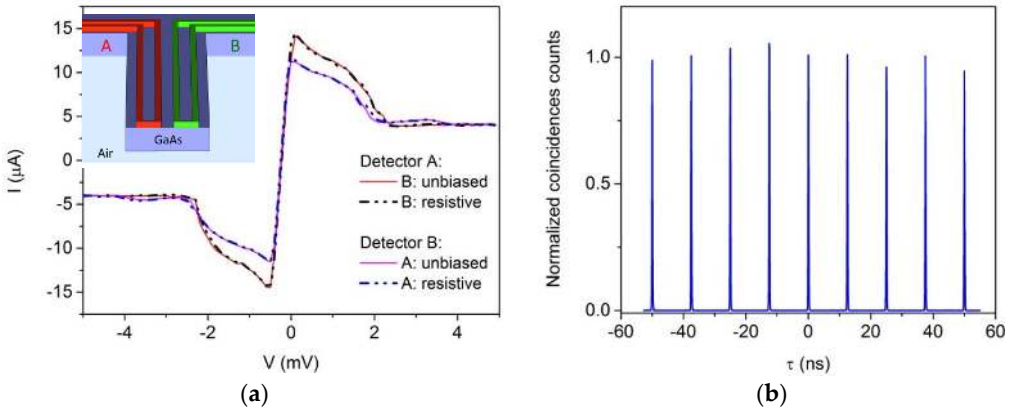

Figure 5. (**a**) I-V curve of Detector A while Detector B is unbiased or in resistive state; I-V curve of Detector B while Detector A is unbiased or in resistive state. Inset: sketch of the two independent SSPDs on top of SNB. (**b**) Coincidence rate under illumination with a 80 MHz pulsed laser at 965 nm and detectors biased at 97% I_c.

Biasing the other detector in the resistive region is a stringent test to prove the absence of static crosstalk. Indeed, the heat dissipated due to Joule effect could thermally affect the other detector, as has been observed for other substrates like sapphire [29]. Instead, it can be clearly seen how the I-V curve are completely superposed in every electrical regime of the device, proving the absence of static crosstalk. The difference between the I_c values (2.7 μA) of the two nominally identical detectors is an indication that, for 20-μm-long wires, the inhomogeneities still play a role [22]. We then tested the existence of dynamic crosstalk. In this test, the temporal variation of the detection probability of one detector due to the firing of the other detector is investigated. If the probability to click after a detection event on the other wire was increased or decreased, $g^{(2)}(\tau)$ would show a peak or a dip

at $\tau = 0$ even in the case of laser illumination. To this end, we measured the intensity correlation function $g^{(2)}(\tau)$ of a pulsed laser (λ = 965 nm, 80 MHz repetition rate) coupled to the waveguide. The detectors were biased at $I_b = 0.97I_c$, and the coincidence counts were measured by sending their outputs to the inputs of a correlation card (PicoHarp 300) using a line with a known delay. In Figure 5b, the coincidence counts are shown as a function of the delay time between the start and stop channels, and as expected coincidences are observed only at delays multiple of the repetition period of the laser (12.5 ns). The coincidence counts are normalized to the average of the peak's maximum presented in Figure 5b and show a standard deviation of 0.03 due to statistical fluctuation. Considering that the peak at zero delay has 1.00 normalized coincidences, it is fair to conclude that no sign of dynamic crosstalk was observed.

3.2. QD Emission

On-Chip Detection

The next step toward the demonstration of a fully functional QPIC is to prove that the SSPDs are able to detect only the light coming from the QDs and not from other sources such as the direct or scattered light of the laser pump. For this low-temperature (2.2 K) measurement, a 750 nm gain switched diode laser with a repetition rate of 80 MHz was used to excite the QDs and use them as an internal light source. The SSPD on SNB was biased at $0.94I_c$, and the output was sent to the correlation card together with the laser trigger to record the coincidences counts. In the first measurement, the instrument response function (IRF) of the SSPD under direct laser illumination at normal incidence with 30 nW of power was measured. The IRF (Figure 6; blue curve) shows a main peak and a shoulder, which may be due to a relaxation oscillation of the laser. A Gaussian fit to the main peak has a FWHM of 134 $\pm$ 4 ps, which corresponds very well to the value of jitter previously measured for the SSPD on a sample without QDs. At long delay, it was possible to recognize a shoulder due to the response to QD emission. The exponential decay fit of the shoulder (green curve) yielded a decay time value $\tau_d = 0.94 \pm 0.01$ ns, which corresponds to the typical spontaneous emission lifetime of these InAs quantum dots [30]. In the second measurement, an ensemble of QDs at the edge of the ridge waveguide (0.5 mm away from the SSPD) was excited non-resonantly with the same power, and the on-chip time resolved photoluminescence (PL) data were recorded (Figure 6; black curve). The exponential fit of the decay time yielded a value $\tau_d = 0.92 \pm 0.01$ ns, in good agreement with the decay time observed in the shoulder on the IRF curve. This proves that, whenever the excitation spot is far enough from the detector, the laser is completely absorbed in the GaAs so that only the QD emission is detected.

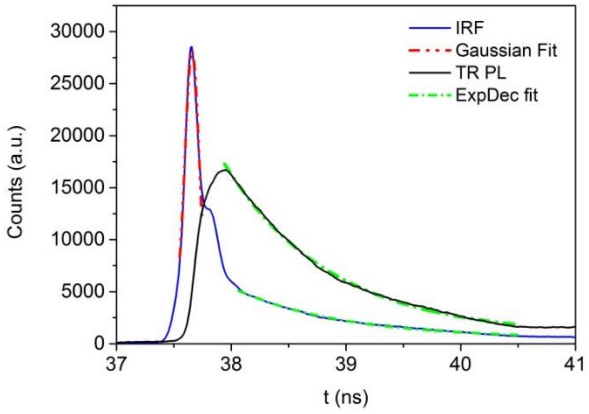

Figure 6. Instrument response function (IRF) of the SSPD (blue) and on-chip time resolve QD photoluminescence measurement (black). The red line represents the Gaussian fit of the IRF and the green lines the exponential fit of the decay time of the QD emission.

3.3. Filters

3.3.1. Design

In order to obtain single-photon emission from QDs, a single excitonic line must be filtered out of the complex emission spectrum of one or more QDs. A coupled PhCC-PhCWG system has been theoretically and experimentally investigated and proposed as a system capable of realizing the filtering functionality [31,32]. Indeed, when the wavelength of the input light matches the wavelength of the cavity, light can pass through the cavity via resonant tunneling. The performance of this filter can be described by coupled-mode theory [33]. The coupling of the cavity to the PhCWG and to the leaky radiation modes can be characterized by quality factors Q_{WG} and Q_R, where the total quality factor Q_T is obtained from $1/Q_T = 1/Q_{WG} + 1/Q_R$, and the transmission is calculated as $T = [1/(1 + Q_{WG}/Q_R)]^2$. This means that for a fixed Q_R (which depends on the design and fabrication of the cavity), increasing the transmission requires a decrease of the Q_{WG}, which will increase the bandwidth of the filter, thus deteriorating the filtering functionality. Therefore, to achieve good filtering performances, a trade-off between the transmission and the bandwidth is required. As the typical spectral separation between lines when few QDs are pumped is in the order of a few nm, we aimed at $Q_T \approx 1000$. Together with a Q_R about equal to 10,000, this should ensure good filtering and high transmission. Another important parameter is the free spectral range (FSR) around the transmission peak: all the QDs with a wavelength different from the cavity must be filtered, so a large FSR is necessary (at least 40 nm). Designs with different coupling between the PhCC and the PhCWG have been simulated. A direct coupling (in-line) of an L3 PhCC (obtained by removing the first three holes from the center of the PhC) with a PhCWG, and a two-hole barrier in between, was found to be the design that best fulfills the requirements (Figure 7 inset). Moreover, the diameter of the external hole of the barrier was reduced by 10%, compared with the others holes, to increase Q. Figure 7 shows the simulated transmissions spectra: both the fundamental and second mode peaks are quite narrow with Q = 1170 and Q = 1230, respectively, and are well separated, resulting in a FSR of 75 nm. The fundamental mode has a transmission of 58%, while the second mode a transmission of 78%.

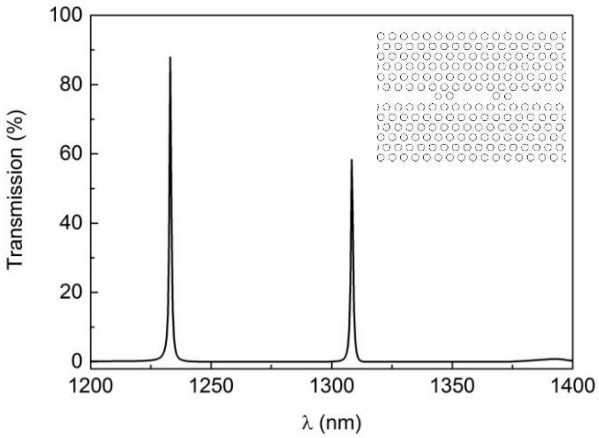

Figure 7. Simulated transmission spectra. Inset: sketch of the chosen design.

3.3.2. Performance

Filters according to the chosen design were fabricated and the transmission spectra were experimentally measured at room temperature using two techniques. First, a non-resonant laser (780 nm) was applied from the top on the two sides of the cavity (Figure 8a; red and blue arrows) and directly on top of it (black arrow). The PL coupled to the PhCWG (green arrow) was collected from the RWG through a lensed fiber. Figure 8b shows side-collection spectra of the PL signal when the laser was focused on top of the cavity and on the two sides. The blue curve (after cavity) shows a broad

emission with several peaks in the slow-light part of the dispersion curve of the PhCWG mode [12], while in the other two it is possible to observe the filtered cavity mode (1266 nm) located around 20 nm away from the slow-light dispersion edge. When the pump was applied on top of the PhCC, some additional peaks were observed, compared with the case where the laser was applied before the PhCC, due to the excitation of the PhCWG section around the cavity (since the laser spot is bigger than the area of the cavity). From the Lorentz fit of the cavity mode, a Q of 1000 was obtained, a value close to the one predicted by the simulation. In the spectra before the cavity (red curve) for the full range of wavelengths (1200–1350 nm; not shown), no other cavity peak was observed, indicating that a FSR of at least 66 nm was obtained.

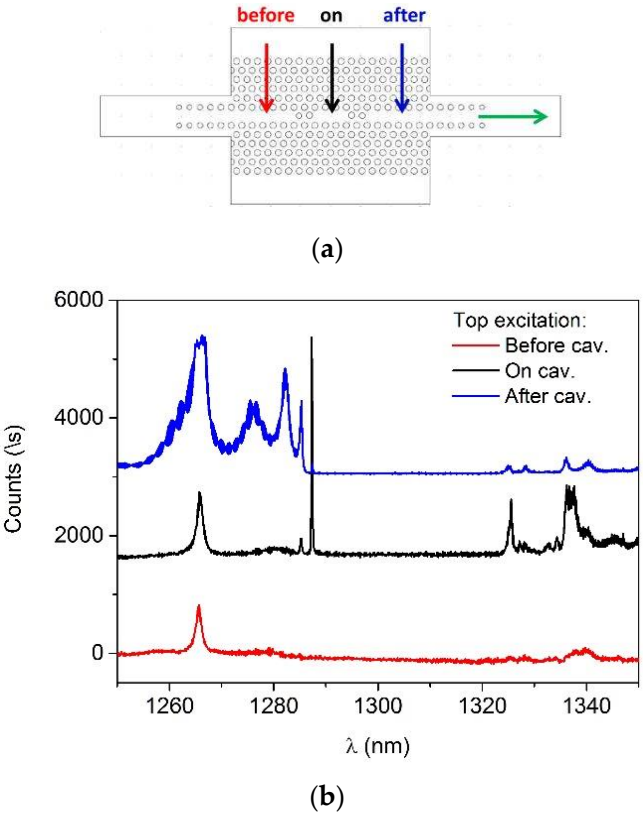

Figure 8. (**a**) Sketch of the design B filter: the red (before cavity), black (on cavity), and blue (after cavity) arrows indicate the different position of the top excitation, while the green the direction of the side collection. (**b**) PL spectra for the three different excitation positions with color coding corresponding to (a). The blue spectra has been reduced by a factor of 5 for greater clarity.

The transmission spectrum shown in black in Figure 9 was calculated as the ratio between the PL spectra acquired from the two sides of the cavity, therefore before and after filtering. The peaks were modulated by Fabry-Perot fringes due to reflections at the cleaved facet and at the interface between RWG and SNB. A clear transmission peak at the same wavelength of the cavity mode was easily distinguishable and well isolated, confirming a very large FSR, although the transmission was only 21% ± 2%. Secondly, a direct measure of transmission was taken using a PhCC-PhCWG coupled with a RWG on both sides, performing a fiber-in:fiber-out measurement with a tunable laser. Considering a coupling efficiency of η_c = 2.5%, the obtained transmission for this measurement was equal to 18% ± 2%.

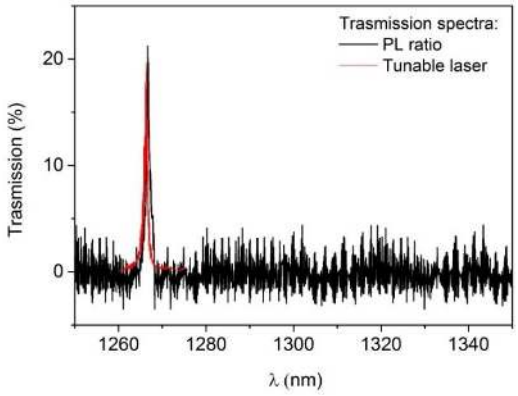

Figure 9. Experimental transmission spectra: black curve indirectly calculated from the ratio between the photoluminescence (PL) spectra before and after filtering, red curve from direct fiber-in:fiber-out measurement.

3.3.3. Filtering of Single QD Lines

Finally, the capability of the on-chip filter to isolate a single QD excitonic line is presented. In Figure 10, two PL spectra measured at low temperature (2.2 K) are shown for side collection when the laser is focused either on top of the cavity or on top of the SNB before the cavity. To be able to better discriminate the single QD excitonic emission line, the pump laser power was strongly attenuated (20 nW). In this particular case, a QD was emitting (1194 nm) exactly within the bandwidth of the cavity mode; therefore, a single excitonic line was passing through the filter while all the other QDs emission lines at different wavelengths were suppressed. However, due to the lower Q = 200 of this specific cavity, some residual QD emission close to the filtered line was not yet well suppressed.

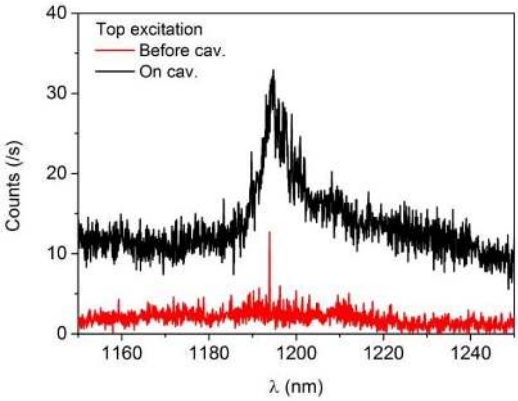

Figure 10. PL spectra on two different excitation position following the previous color coding. A single QD excitonic line is clearly visible on the red curve.

4. Discussion

The low temperature fabrication process, developed in order to integrate single-photon sources and detectors on a GaAs platform, has shown an ability to preserve high performance for each component of the proposed QPIC. In particular, the SSPD patterned on top of a SNB presents a DQE of 28% and a jitter of 127 $\pm$ 8 ps. The simulation of the electric field mode guided inside the SNB showed the possibility of using shorter wires (15-µm-long), preserving high absorptance (90%) and thereby reducing the inhomogeneities problem. Even if the experimental DQE did not improve as much as expected, a new record for the DQE on the GaAs platform has been established. Autocorrelators based on two electrically independent SSPDs on top of a SNB did not present any static or dynamic crosstalk; this, together with a jitter much shorter than the QD lifetime, shows that the integrated

autocorrelators are suitable for the on-chip measurement of single-photon emission. On the other hand, the PhCC-PhCWG system showed the expected filtering functionality of a single-excitonic line. From the experimental transmission spectra, a FSR $\geq$ 66 nm and Q = 1000, as estimated from the simulation, were found; however, the transmission was 21% lower than expected, presumably due to disorder-induced optical losses. Even with such transmission, it has been possible to prove that single excitonic lines can be isolated and transmitted through the filter. Moreover, it has been proved that the QD emission can be detected by the on-chip SSPDs, whenever the laser is focused at a sufficiently long distance from the detector. In conclusion, a platform able to combine QD sources, filters, detectors, and autocorrelators has been developed and successfully tested, paving the way for numerous QIP applications.

Acknowledgments: This research is financially supported by the European Commission, Initial Training Network PICQUE (No. 608062), by the Dutch Technology Foundation STW, Applied Science Division of NWO, the Technology Program of the Ministry of Economic Affairs under projects No. 10380, 12662 and by NanoNextNL, a micro and nanotechnology program of the Dutch Ministry of Economic Affairs, Agriculture and Innovation (EL&I) and 130 partners.

Author Contributions: G.E.D., M.P. and A.F. conceived and designed the experiment, F.W.M.v.O. grew the wafer and G.E.D. with the contribution of R.G. and M.P. fabricated the devices. M.P. with the contribution of S.F.P. developed the simulation. G.E.D., M.P. and S.B. performed the experiments. G.E.D. analyzed the data and wrote the paper. A.F. supervised the project.

Conflicts of Interest: The authors declare no conflict of interest.

References

1. O'Brien, J.L. Optical quantum computing. *Science* **2007**, *318*, 1567–1570. [CrossRef] [PubMed]
2. O'Brien, J.L.; Fusawa, A.; Vuckovic, J. Photonic quantum technologies. *Nat. Phys.* **2009**, *3*, 687–695. [CrossRef]
3. Dietrich, C.P.; Fiore, A.; Thompson, M.G.; Kamp, M.; Hofling, S. GaAs integrated quantum photonics: Towards compact and multi-functional quantum photonic integrated circuits. **2016**, arXiv:1601.06956v2.
4. Shields, A.J. Semiconductor quantum light sources. *Nat. Photonics* **2007**, *1*, 215–223. [CrossRef]
5. Englund, D.; Faraon, A.; Zhang, B.; Yamamoto, Y.; Vucković, J. Generation and transfer of single photons on a photonic crystal chip. *Opt. Express* **2007**, *15*, 5550–5558. [CrossRef] [PubMed]
6. Schwagmann, A.; Kalliakos, S.; Farrer, I.; Griffiths, J.P.; Jones, G.A.C.; Ritchie, D.A.; Shields, A.J. On-chip single photon emission from an integrated semiconductor quantum dot into a photonic crystal waveguide. *Appl. Phys. Lett.* **2011**, *99*, 261108. [CrossRef]
7. Laucht, A.; Pütz, S.; Günthner, T.; Hauke, N.; Saive, R.; Frédérick, S.; Bichler, M.; Amann, M.-C.; Holleitner, A.W.; Kaniber, M.; et al. A waveguide-coupled on-chip single-photon source. *Phys. Rev. X* **2012**, *2*, 011014. [CrossRef]
8. Hoang, T.B.; Midolo, L.; Dietrich, C.P.; Li, L.H.; Linfield, E.H.; Schouwenberg, J.F.P.; Xia, T.; Pagliano, F.M.; van Otten, F.W.M.; Fiore, A. Efficient coupling of single photons to ridge-waveguide photonic integrated circuits. *Appl. Phys. Lett.* **2013**, *102*, 131105.
9. Tanzilli, S.; de Riedmatten, H.; Zbinden, H.; Baldi, P.; de Micheli, M.; Ostrowsky, D.; Gisin, N. Highly efficient photon-pair source using periodically poled lithium niobate waveguide. *Electron. Lett.* **2001**, *37*, 26–28. [CrossRef]
10. Sharping, J.E.; Lee, K.F.; Foster, M.A.; Turner, A.C.; Schmidt, B.S.; Lipson, M.; Gaeta, A.L.; Kumar, P. Generation of correlated photons in nanoscale silicon waveguides. *Opt. Express* **2006**, *14*, 12388–12393. [CrossRef] [PubMed]
11. Patel, R.B.; Bennett, A.J.; Farrer, I.; Nicoll, C.A.; Shields, A.J. Two-photon interference of the emission from electrically tunable remote quantum dots. *Nat. Photonics* **2010**, *4*, 632–635. [CrossRef]
12. Hoang, T.B.; Beetz, J.; Lermer, M.; Midolo, L.; Kamp, M.; Höfling, S.; Fiore, A. Widely tunable, efficient on-chip single photon sources at telecommunication wavelengths. *Opt. Express* **2012**, *20*, 21758–21765. [CrossRef] [PubMed]
13. Midolo, L.; Pagliano, F.; Hoang, T.B.; Xia, T.; van Otten, F.W.M.; Li, L.H.; Linfield, E.H.; Lermer, M.; Hofling, S.; Fiore, A. Spontaneous emission control of single quantum dots by electromechanical tuning of a photonic crystal cavity. *Appl. Phys. Lett.* **2012**, *101*, 091106. [CrossRef]

14. Petruzzella, M.; Xia, T.; Pagliano, F.; Birindelli, S.; Midolo, L.; Zobenica, Z.; Li, L.H.; Linfield, E.H.; Fiore, A. Fully tuneable, Purcell-enhanced solid-state quantum emitters. *Appl. Phys. Lett.* **2015**, *107*, 141109. [CrossRef]
15. Gol'tsman, G.N.; Okunev, O.; Chulkova, G.; Lipatov, A.; Semenov, A.; Smirnov, K.; Voronov, B.; Dzardanov, A.; Williams, C.; Sobolewski, R. Picosecond superconducting single-photon optical detector. *Appl. Phys. Lett.* **2001**, *79*, 705–707. [CrossRef]
16. Natarajan, C.M.; Tanner, M.G.; Hadfield, R.H. Superconducting nanowire single-photon detectors: Physic and application. *Supercond. Sci. Technol.* **2012**, *25*, 063001. [CrossRef]
17. Sprengers, J.; Gaggero, A.; Sahin, D.; Jahanmirinejad, S.; Frucci, G.; Mattioli, F.; Leoni, R.; Beetz, J.; Lermer, M.; Kamp, M.; et al. Waveguide superconducting single-photon detectors for integrated quantum photonic circuits. *Appl. Phys. Lett.* **2011**, *99*, 181110. [CrossRef]
18. Kaniber, M.; Flassig, F.; Reithmaier, G.; Gross, R.; Finley, J.J. Integrated superconducting detectors on semiconductors for quantum optics application. *Appl. Phys. B* **2016**, *22*, 1–10. [CrossRef]
19. Pernice, W.H.P.; Schuck, C.; Minaeva, O.; Li, M.; Goltsman, G.N.; Sergienko, A.V.; Than, H.X. High-speed and high-efficiency travelling wave single-photon detectors embedded in nanophotonic circuits. *Nat. Commun.* **2012**, *3*, 1325. [CrossRef] [PubMed]
20. Akhlaghi, M.K.; Schelew, E.; Young, J.F. Waveguide integrated superconducting single photon detectors implemented as coherent perfect absorbers. **2014**, arXiv:1409.1962v1.
21. Sahin, D.; Gaggero, A.; Weber, J.W.; Agafonov, I.; Verheijen, M.A.; Mattioli, F.; Beetz, J.; Kamp, M.; Höfling, S.; van de Sanden, M.C.M.; et al. Waveguide nanowire superconducting single-photon detectors fabricated on GaAs and the study of their optical properties. *IEEE J. Sel. Top. Quant. Electron.* **2015**, *21*, 1–10. [CrossRef]
22. Gaudio, R.; Op't Hoog, K.P.M.; Zhou, Z.; Sahin, D.; Fiore, A. Inhomogeneous critical current in nanowire superconducting single-photon detectors. *Appl. Phys. Lett.* **2014**, *105*, 222602. [CrossRef]
23. Sahin, D.; Gaggero, A.; Hoang, T.B.; Frucci, G.; Mattioli, F.; Leoni, R.; Beetz, J.; Lermer, M.; Kamp, M.; Höfling, S.; Fiore, A. Integrated autocorrelator based on superconducting nanowires. *Opt. Express* **2013**, *21*, 11162–11170. [CrossRef] [PubMed]
24. Brown, R.H.; Twiss, R. A test of a new type of stellar interferometer on Sirius. *Nature* **1956**, *178*, 1046–1048. [CrossRef]
25. Gaggero, A.; Nejad, S.J.; Marsili, F.; Mattioli, F.; Leoni, R.; Bitauld, D.; Sahin, D.; Hamhuis, G.J.; Nötzel, R.; Sanjines, R.; et al. Nanowire superconducting single-photon detectors on GaAs for integrated quantum photonic applications. *Appl. Phys. Lett.* **2010**, *97*, 151108. [CrossRef]
26. Li, L.H.; Chauvin, N.; Patriarche, G.; Alloing, B.; Fiore, A. Growth-interruption-induced low-density InAs quantum dots on GaAs. *J. Appl. Phys.* **2008**, *104*, 083508. [CrossRef]
27. Clem, J.R.; Berggren, K.K. Geometry-dependent critical currents in superconducting nanocircuits. *Phys. Rev. B* **2011**, *17*, 174510. [CrossRef]
28. Marsili, F.; Bitauld, D.; Gaggero, A.; Jahanmirinejad, S.; Leoni, R.; Mattioli, F.; Fiore, A. Physics and application of photon number resolving detectors based on superconducting parallel nanowires. *New J. Phys.* **2009**, *11*, 045022. [CrossRef]
29. Dauler, E.A.; Robinson, B.S.; Kerman, A.J.; Yang, J.K.; Rosfjord, E.; Anant, V.; Voronov, B.; Gol'tsman, G.; Berggren, K.K. Multi-element superconducting nanowire single-photon detector. *IEEE Trans. Appl. Supercond.* **2007**, *17*, 279–284. [CrossRef]
30. Zinoni, C.; Alloing, B.; Monat, C.; Zwiller, V.; Li, L.H.; Fiore, A.; Lunghi, L.; Gerardino, A.; de Riedmatten, H.; Zbinden, H.; Gisin, N. Time-resolved and antibunching experiment on single quantum dots at 1300 nm. *Appl. Phys. Lett.* **2006**, *88*, 131102. [CrossRef]
31. Takano, H.; Akahane, Y.; Asano, T.; Noda, S. In plan-type channel drop filter in a two-dimensinal photonic crystal slab. *Appl. Phys. Lett.* **2004**, *24*, 2226. [CrossRef]
32. Moosburger, J.; Kamp, M.; Forchel, A.; Oesterle, U.; Houdre, R. Trasmission spectroscopy of photonic crystal based waveguides with resonant cavities. *J. Appl. Phys.* **2002**, *91*, 4791–4794. [CrossRef]
33. Joannopoulos, J.D.; Johnson, S.G.; Winn, J.N.; Meade, R.D. *Photonic Crystal Molding the Flow of Light*, 3rd ed.; Princeton University Press: Princeton, NJ, USA, 2008.